HiSST: 3rd International Conference on
High-Speed Vehicle Science Technology
14 -19 April 2024, Busan, Korea

First Hot Combustion Subsonic Retro Propulsion Tests in the Vertical Free Jet Facility Cologne (VMK)

Ansgar Marwege[1], Daniel Kirchheck[1], Ali Gülhan[1]

Abstract

High uncertainties exist in modelling subsonic retro propulsion flow fields with CFD. For example, the choice of the turbulence model can greatly influence the flow field and the resulting heat loads. Hence, experiments with hot oxygen/hydrogen exhaust plumes and active counterflow are indispensable for the understanding of these flow fields. In the frame of the Horizon 2020 project RETALT, first subsonic retro propulsion experiments with oxygen/hydrogen combustion have been performed in the Hot Plume Testing Facility (HTPF) which consists of the Vertical Free Jet Facility Cologne (VMK) and an oxygen/hydrogen supply infrastructure. Oxidizer fuel ratios of around 0.7 were tested at Mach numbers of 0.6, 0.7, 0.8 and 0.9. The stagnation pressures in the model were around 21 bar. The steady and unsteady flow field features were analysed with regular video recordings, schlieren and infrared recordings. Furthermore, the pressures and temperatures in the base area were evaluated. The tests are compared to earlier cold gas tests of the same configuration. The steady flow field features are similar to those in cold gas test. However, the unsteady features prove to be very different. A general tendency of the dependence of the plume length on the momentum flux ratio, found in could gas tests, can be confirmed. However, the plume length is larger in the hot tests. The dominant frequencies found in cold gas tests in the modes of the Schlieren recordings differ from those found in the hot gas tests. Due to current trends in the European launcher designs towards the use of oxygen/methane engines, in the future, methane experiments are foreseen and an improved model concept shall enable higher oxidizer fuel ratios and, therefore, a better similarity to the flight conditions.

Keywords: *subsonic retro propulsion, hot plume testing, wind tunnel tests, oxygen/hydrogen, Hot Plume Testing Facility*

Nomenclature

APR – Ambient Pressure Ratio
DRL – Down Range Landing
GTO – Geostationary Transfer Orbit
HPTF – Hot Plume Testing Facility
MECO – Main Engine Cut-off
MFR – Momentum Flux Ratio
OFR – Oxidizer Fuel Ratio
POD – Proper Orthogonal Decomposition
RTLS – Return to Launch Site
RETALT – Retro Propulsion Assisted Landing Technologies
VMK – Vertical Free Jet Facility Cologne
SRP – Supersonic Retro Propulsion

1. Introduction

Since the first retro propulsion assisted vertical landing by the SpaceX Falcon 9 launch vehicle in 2015, great interest exists in Europe to master this technology. Due to the possible reusability of the first stage of the launch vehicle, this technology promises significant costs savings.
A comparable configuration, RETALT1, with a vertical landing first stage was studied in the EU Horizon 2020 project RETALT (grant agreement number 821890). The mission profile for this configuration is shown in Fig. 1. The RETALT1 configuration layout is shown in Fig. 2. It is a heavy lift launch vehicle

[1] *Supersonic and Hypersonic Technologies Department, Institute of Aerodynamics and Flow Technology, German Aerospace Center (DLR e.V.), Linder Hoehe, 51147 Cologne, Germany*

for up to 14 t into the Geostationary Transfer Orbit (GTO). After the ascent phase and stage separation (after the Main Engine Cut-off, MECO), the first stage is recovered. It is either landed downrange on a seagoing platform (Down Range Landing, DRL) or flown back to the launch site (Return to Launch Site, RTLS). [1]
For both mission profiles, a re-entry burn and a landing burn are performed. While the re-entry burn decelerates the vehicle at high altitudes in order to reduce the dynamic pressure and heat loads in the following aerodynamic phase [2], the landing burn decelerates the vehicle to nearly zero velocity for touch down [3].
During the landing burn, a complex flow field, consisting of the hot jet and the counterflowing free stream is observed. Numerical simulations of those flow fields with CFD (Computational Fluid Dynamics) are highly sensitive to the modelling approach. For example, studies performed by Ecker et al. [4] and Ertl et al. [5] showed that the plume length, the flow field appearance and the computed heat loads strongly depend on the choice of the turbulence model.
Hence, in the frame of the European Union Horizon 2020 project RETALT, first experiments were performed using oxygen/hydrogen combustion in a model-integrated combustion chamber to study these flow fields. The tests were performed in the Hot Plume Testing Facility (HPTF) built around the Vertical Free Jet Facility (VMK) at the German Aerospace Center (DLR) in Cologne. The results of these tests are presented here. They are complementary to the cold gas tests performed with the same model in the VMK and presented in reference [6].

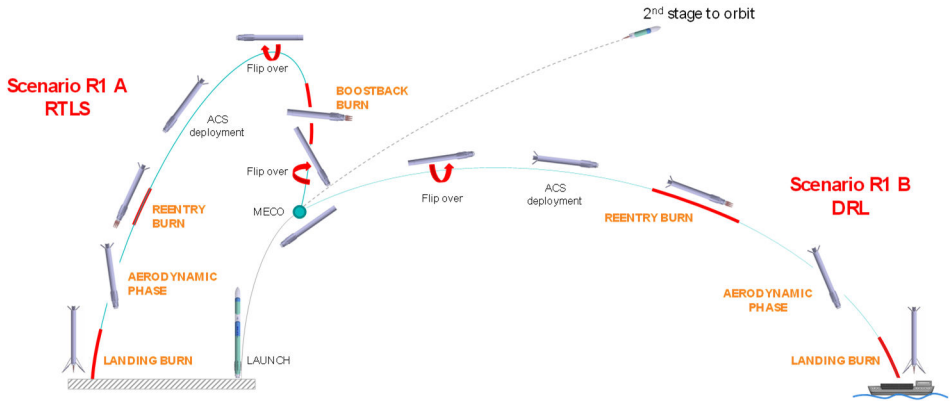

Fig. 1: RETALT1 mission concept [2]

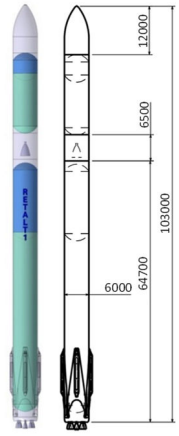

Fig. 2: Outline of the RETALT1 configuration as presented in [1]

2. Subsonic Retro Propulsion

Subsonic retro propulsion refers to a supersonic jet being directed against the subsonic free stream. The flow field appearance is similar to the long penetration mode in Supersonic Retro Propulsion (SRP) flow fields, however due to the absence of the bow shock upstream of the contact surface of the jet with the free stream, the jet extends farther in the free stream and shows a multicell structure [6, 7]. A snapshot of a schlieren recording of the subsonic retro propulsion flow field in a cold gas experiment is shown in Fig. 3. The plume is highly unsteady. Pressure waves radiate away from the contact surface between the free stream and the wake of the jet in the upstream direction. Large pressure fluctuations are created in the wake area of the jet. In [8] it was shown that the plume length depends linearly on the square root of the momentum flux ratio ($MFR = (\rho_e\, u_e^2)/(\rho_\infty\, u_\infty^2)$) as it can be estimated with:

$$\frac{x}{D_e} = 3.1\left(\frac{\rho_e u_e^2}{\rho_\infty u_\infty^2}\right)^{\frac{1}{2}}\left(\frac{T_{CC}}{T_e}\right)^{\frac{1}{2}} = 3.1\; MFR^{\frac{1}{2}}\left(\frac{T_{CC}}{T_e}\right)^{\frac{1}{2}} \qquad (1)$$

where ρ_e, T_e and u_e are the density, the temperature and the velocity at the nozzle exit, T_{cc} is the total temperature in the combustion chamber, and ρ_∞ and u_∞ are the density and velocity in the free stream. This correlation could be confirmed with experimental data by Marwege et al. in [6, 9], but with slightly different constants other than 3.1. Close to the engine nozzle exit, the Ambient Pressure Ratio (APR), $APR = p_e/p_\infty$, is the dominating scaling parameter [6]. As stated the introduction, the

plume length, the flow field appearance and the computed heat loads strongly depend on the choice of the turbulence model [4, 5]. This is why experimental data rebuilding the hot exhaust gas with actual oxygen/hydrogen combustion products are crucial for the understanding of the complex flow fields and for the validation of respective CFD computations.

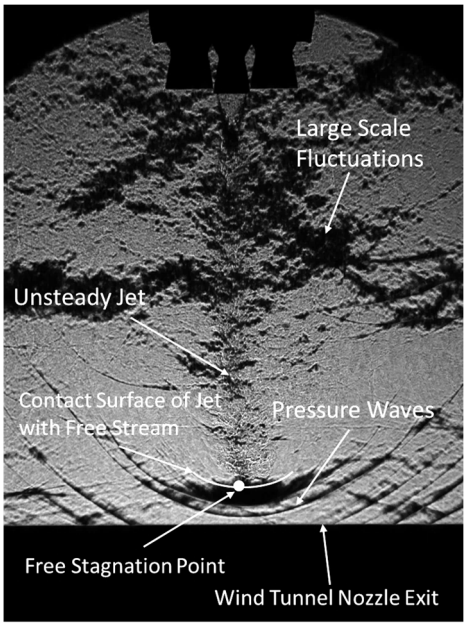

Fig. 3 Snapshot of a schlieren video showing unsteady flow features in a subsonic flow field at Mach 0.8 and $APR = 0.389$ [6] (free stream is pointing form the bottom to the top)

3. Test setup

3.1. Hot Plume Testing Facility (HPTF) and Vertical Free Jet Facility Cologne (VMK)

The Hot Plume Testing Facility (HPTF) is the Vertical Free Jet Facility Cologne (VMK) together with the GH2/GO2 supply facility, which is designed for hot gas investigations in the VMK test environment (see Fig. 4a). [10]

The VMK is a blow-down type wind tunnel with an atmospheric free stream test section in vertical alignment. The maximum operating pressure is 35 bar, which is maintained by a pressure reservoir of 1 000 cubic meters volume at a maximum pressure of 60 bar. The schematic layout of the VMK is shown in Fig. 5a. The reservoir allows typical test durations of 30 to 60 seconds and the upstream heat storage allows to heat-up the flow to 750 Kelvin, which enables testing at ground-level conditions up to a Mach number of 2.8. The flow Mach number is set by various discrete nozzles in the supersonic range up to Mach 3.2. Subsonic conditions are set by a convergent nozzle of 340 millimeter exit diameter. The detailed operating range is given in Fig. 5b. The design of the test chamber is explosion proof and in combination with modern gas monitoring devices, explosion protected electric installations, and gas proof interfaces suitable for the operation of combustion tests with gaseous and solid propellant combinations. For the cold gas interaction tests, a high-pressure dried air supply is available with a maximum supply pressure of 150 bar. [10]

The GH2/GO2 supply facility is an extension to the VMK infrastructure. Fig. 4b shows the operating range of the facility; The infrastructure consists of a 300 bar gas storage for the supply with process gases (hydrogen, oxygen, and nitrogen for purging and inerting purposes) and a control station to set the operating conditions by an integrated mass flow controller. The control station operates at 130 bar and feeds the model combustor with a maximum of 399 g/s oxygen and 67 g/s hydrogen at a maximum chamber pressure of 115 bar. The resulting operating range as a function of chamber pressure p_{CC} and oxidizer fuel ratio (OFR) is given in Fig. 4b as iso-contours of the theoretical chamber temperature T_{CC} (solid lines) and the area specific mass flow rate $\dot{m}/A_{th}$ (dashed lines). The theoretical maximum operating envelope is given by the maximum supply pressure, min./max. mass flow rates, the

theoretical ignition limit OFR > 0.5 and the maximum mass flow ratio OFR < OFR_{st} = 7.918. The model design conditions are commonly reduced to 80 bar at stoichiometric mixture, which results in a common theoretical operating range of the wind tunnel models represented by the filled area in Fig. 4b. [10]

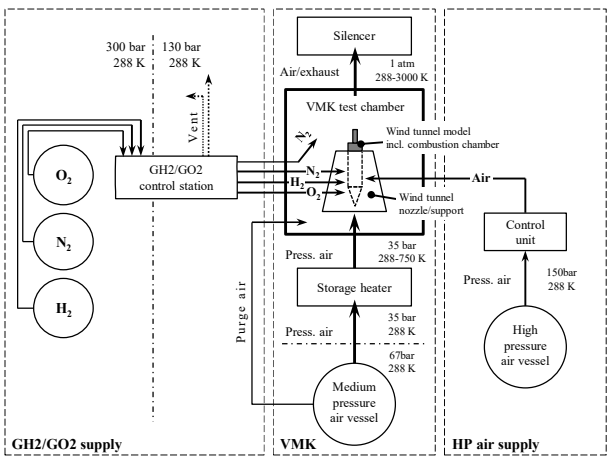

a) Hot Plume Testing Facility (HPTF), consisting of the Vertical Free Jet Facility (VMK), the GH2/GO2 supply facility, and a high-pressure (HP) air supply system [10]

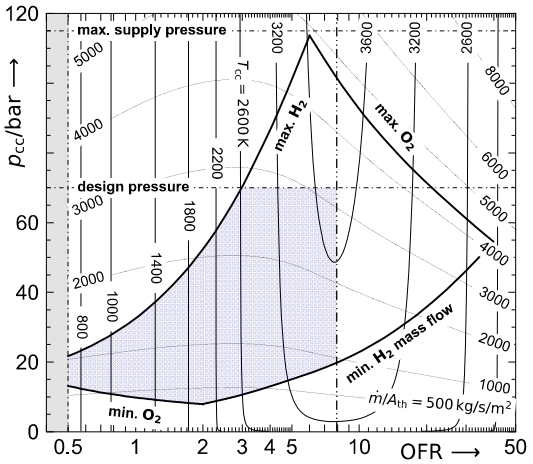

b) Operating range of the GH2/GO2 supply facility in the field of total chamber pressure p_{CC} and oxidizer fuel ratio OFR as maximum operating envelope (thick solid line) and model design envelope (filled area) [10]

Fig. 4: Over view of the Hot Plume Testing Facility (HPTF)

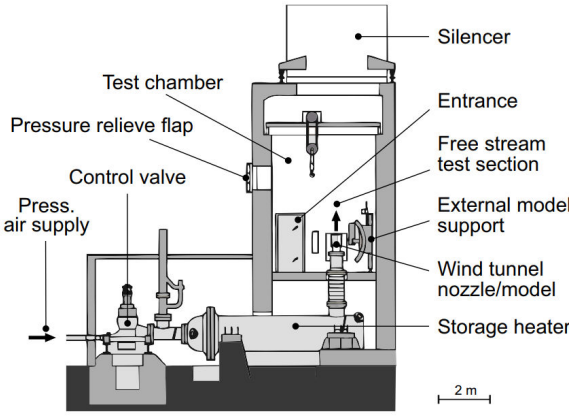

a) Scheme of the VMK facility layout around the test chamber [10]

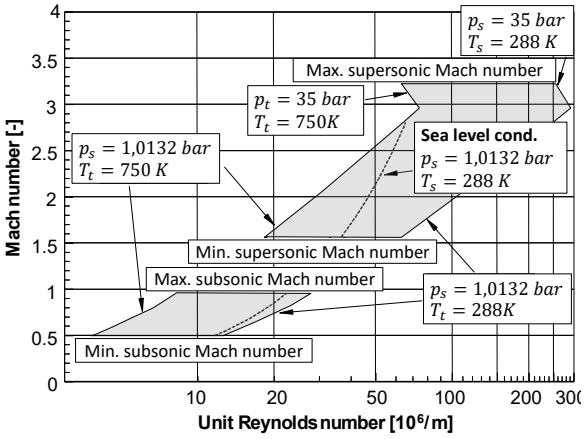

b) Operating range of the facility [10]

Fig. 5: Overview of Vertical Free Jet Facility Cologne (VMK)

3.2. Wind Tunnel Model Design

The test set-up in the VMK is shown in Fig. 6. The wind tunnel model is mounted on a model support and oriented such that the exhaust plume is acting from top to bottom, against the free stream. It is scaled with 7/600 to the flight configuration, which results in a model diameter of 70 mm. The scaling follows a trade-off of best meeting the similarity parameters of the flight conditions, while keeping design restrictions, as e.g. the minimum size required for the combustion chamber integrated for the hot plume experiments. The model is designed for a maximum pressure of 80 bar at a temperature of approx. 1000 K. It contains pressure and temperature measurements. The pressure sensors were exchangeable. This way, testing during hot gas experiments was performed using static pressure sensors, as it was expected that dynamic sensors would not stand the expected high temperatures during the test. However, during cold gas tests, dynamic pressure sensors were used. For the temperature sensors, static sensors were chosen due to spatial limitations in the model base plane. The

positioning of the model in the wind tunnel facility can be adjusted with the movable support drive also shown in Fig. 6. It shall be noted, that the model represents the base part and cylindrical body of the flight configuration.
The wind tunnel model concept is shown in Fig. 7. Gaseous oxygen and hydrogen are supplied in the manifold assembly and injected to the combustion chamber using a single element coaxial shear-flow injector. The combustor concept is derived from the Penn State burner [13], which was already the basis for other hot gas models in former test campaigns in the HPTF by Kirchheck et al. [11]. Internal combustion chamber and injector geometries are similar to those former tests at comparable OFR. Details on the injector design process are provided in Saile et al. [12].
The combustion creates a hot exhaust plume at the model's nozzle exit, being expanded by an expansion area ratio of 5.5 resulting in an exit Mach number of 3.275 (for air), with a throat diameter of 5.45 mm, an exit diameter of 12.77 mm and an exit angle of 5.57°. The exit angle was chosen to be 5.57° to match the nozzle exit angle of the RETALT1 first stage engine which has a thrust optimized contour with an area expansion ratio of 15 [6]. The positioning of the model in the wind tunnel facility can be adjusted with the movable support drive. Especially the wind tunnel model nozzle is exposed to high heat loads during the tests and has a small wall thickness of just 1.4 mm. For this reason, cooling ducts were included in the nozzle, which are shown in Fig. 8. The eight engines which are not acting during the landing burn were designed as dummy nozzles, which were removable to test their influence on the flow field.

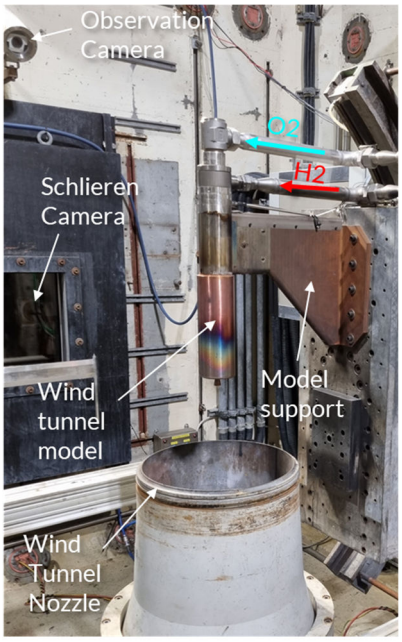

Fig. 6: Test Set-up in VMK for hot gas tests

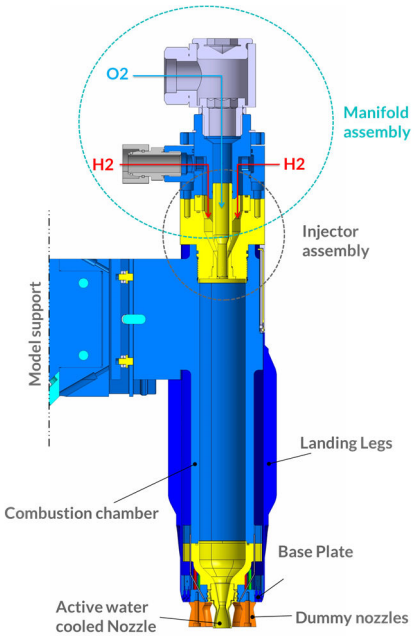

Fig. 7: Model concept for RETALT1 hot combustion wind tunnel model for VMK tests

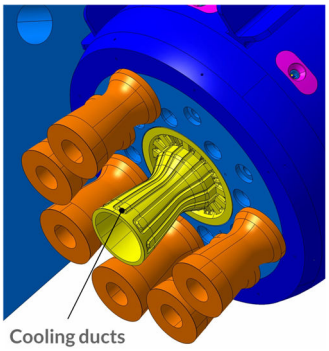

Fig. 8: Central nozzle with transparent view on cooling ducts

Preparatory experiments showed that high heat loads can be observed on the landing leg cover in the hot gas experiments. As the experiments are performed at low OFRs, hydrogen excess is present in the exhaust plume. The incoming free stream supplies a large amount of oxygen leading to strong post combustion. To avoid heat load peaks in the cover it was redesigned for the hot gas experiments as shown in Fig. 9. The cover was manufactured out of copper due to its large heat capacity, acceptable melting temperature and particularly due to its very high heat conductivity. Therefore, the heat loads can be distributed equally over the cover in a short time and the cover itself has enough heat capacity to cope with the integral heat loads.

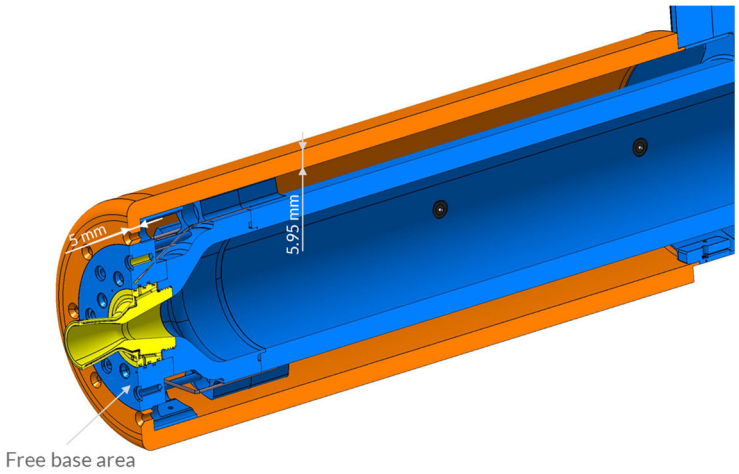

Fig. 9. Outer cover for high heat loads

3.3. Wind Tunnel Model Instrumentation

The wind tunnel model was instrumented with 7 temperature sensors in the combustion chamber, which were positioned inside the chamber wall (Fig. 13, 1–7). The positions 8–10, reaching directly into the chamber were not instrumented. Also, the total chamber pressure and the inflow/outflow nozzle water cooling temperature were measured (Fig. 11).

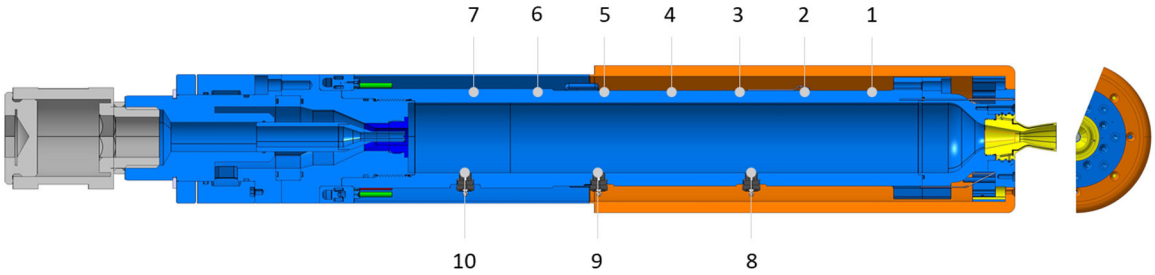

Fig. 10: Temperature Measurements in the combustion chamber

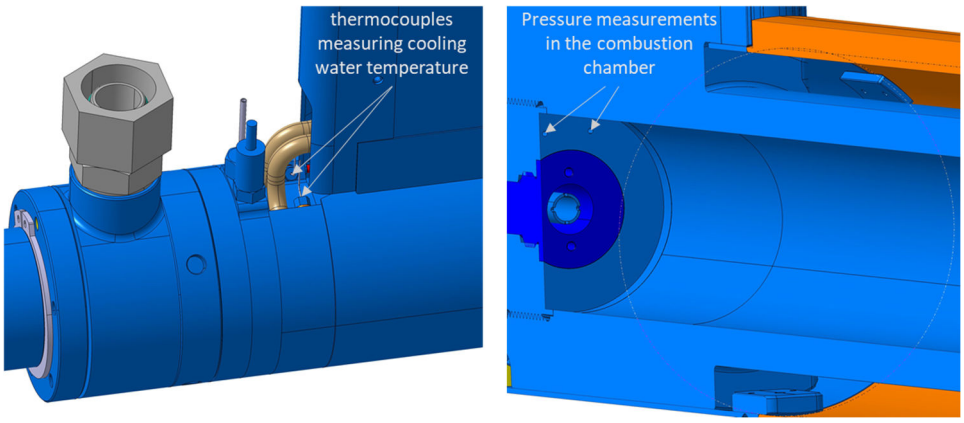

Fig. 11: Temperature measurements of cooling water for the model's nozzle cooling (left) and pressure measurements in combustion chamber (right)

The instrumentation layout for the base area is shown in Fig. 12, where Fig. 12a shows a map of the sensor locations and Fig. 12b shows the sensors relative to the wind tunnel model. In the cold tests the outer two rings (denoted 2 and 3) were instrumented with high frequency pressure transducers (Kulite XCQ-080-3.5BARA and XCE-080-3.5BARA). As the redesigned copper cover was mounted in the hot tests, here, only static pressure measurements at the inner rings (denoted 0 and 1) were performed. While in the cold gas tests, the dummy nozzles were used, a simplified axisymmetric configuration

without dummy nozzles was used for the hot gas tests. In the cold gas tests, also the pressure on the cylindrical part was instrumented with a high frequency pressure sensor (L6 in Fig. 13).

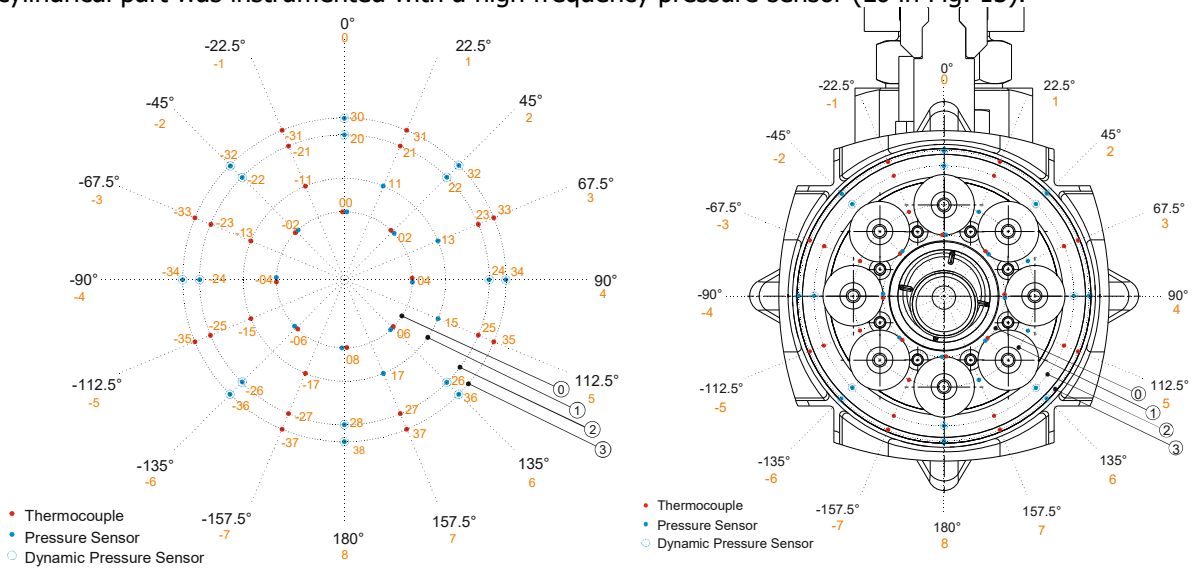

a) Map of sensor locations **b) Locations on the wind tunnel model**

Fig. 12: Sensor locations for thermocouples and pressure sensors on the base

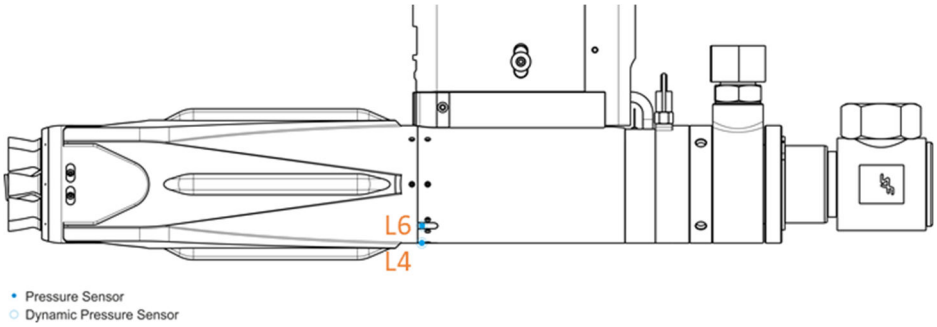

Fig. 13: Sensors along the cylindrical body of the wind tunnel model

3.4. Nozzle Design for the Wind Tunnel Model

The dominating similarity parameters for the large scale flow features in the subsonic retro propulsion flows, like the plume length, is the momentum flux ratio (MFR) [6, 8]. The MFR and the vacuum thrust coefficient, where the pressure loss is neglected, can be used interchangeably [6, 11]. Furthermore, the ambient pressure ratio (APR) is a second prevailing similarity parameter [6].

The vacuum thrust coefficient and the APR were also used for the nozzle design of the wind tunnel model for H2K. The scaling procedure is described in detail in reference [15]. The same strategy was used here and will be discussed in the following.

Tab. 1 shows the two test conditions for which the wind tunnel model nozzles were sized. One condition at Mach 0.4 and one at Mach 0.8. As the VMK is a free-jet facility, the static pressure in the free stream, p_∞, can be assumed to be approximately 1 bar.

The engine scaling parameter K is defined as [12, 13]:

$$\mathrm{K} = \frac{\gamma_\infty}{2}\frac{A_B}{A_e}\frac{1}{1+\gamma_e M_e^2} \qquad (2)$$

Where C_T is the thrust coefficient, M_∞ and M_e are the freestream and nozzle exit Mach numbers, A_e is the nozzle exit area, and γ_e and γ_∞ are the heat capacity ratios at the nozzle exit and in the freestream. The ratio of the thrust coefficients in the experiment and in the flight configuration can then be expressed as [13]:

$$\underbrace{\frac{C_{T,exp}}{C_{T,Fl}}}_{\substack{Thrust\ coefficient\\ similarity}} = \underbrace{\frac{M_{\infty,Fl}^2}{M_{\infty,exp}^2}}_{\substack{Mach\ number\\ similarity}} \cdot \underbrace{\frac{\left(\frac{p_e}{p_\infty}\right)_{exp}}{\left(\frac{p_e}{p_\infty}\right)_{Fl}}}_{\substack{Ambient\ pressure\\ ratio\ similarity}} \cdot \underbrace{\frac{\mathrm{K}_{Fl}}{\mathrm{K}_{exp}}}_{\substack{Engine\ scaling\\ parameter\ ratio}} \quad (3)$$

Where the subscripts exp and Fl stand for the experimental and the flight configuration respectively. Hence, the ratio of the thrust coefficient of the experiment to the flight configuration with the subscript exp/Fl is proportional to the inverse of the engine scaling parameter, if $M_{\infty,Fl/exp}^2 = 1$ and $\left(\frac{p_e}{p_\infty}\right)_{exp/Fl} = 1$ [13]:

$$C_{T,exp/Fl} = \frac{1}{\mathrm{K}_{exp/Fl}} \quad (4)$$

Consequently for $M_{\infty,Fl/exp}^2 = 1$ and $C_{T,exp/Fl} = 1$ follows that the APR ratio is proportional to the engine scaling parameter [13]:

$$\left(\frac{p_e}{p_\infty}\right)_{exp/Fl} = \mathrm{K}_{exp/Fl} \quad (5)$$

Computing the engine scaling parameter for several expansion area ratios and with equation (4) and (5), the thrust coefficient and APR similarities can be plotted depending on the expansion area ratio as shown in Fig. 14. It can be seen that at an expansion area ratio of 5.5 both similarities can be matched at the same time. It shall be noted that this plot is the same for the VMK as for the H2K wind tunnel model described in [13]. As the engine scaling parameter only depends on the engine conditions and γ_∞, the optimal expansion ratio to match the thrust coefficient and the APR at the same time is independent of the wind tunnel free stream conditions as long as the same free stream gas with the same γ_∞ is used.

Fig. 15 and Fig. 16 show the pressures in the model, necessary to reach the similarities. As the static pressure in flight is much lower for the higher altitude of the Mach 0.8 condition, the APR and thrust coefficients are much higher for this condition and, hence, a much higher pressure is needed in the wind tunnel model to achieve the similarity. The pressure for the Mach 0.4 condition is in the range of the maximum combustion chamber pressure of 80 bars. Therefore, an expansion ratio of 5.5 was chosen to reach similarity for the lower Mach numbers.

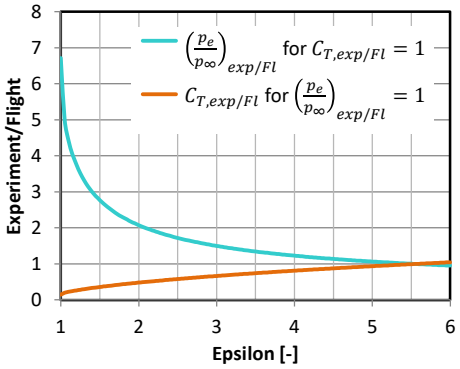

Fig. 14: Exit pressure ratio similarity and thrust coefficient similarity as function of the nozzle expansion area ratio as in eq. (4) and (6) (for $M_{\infty,Fl/exp}^2 = 1$). [13]

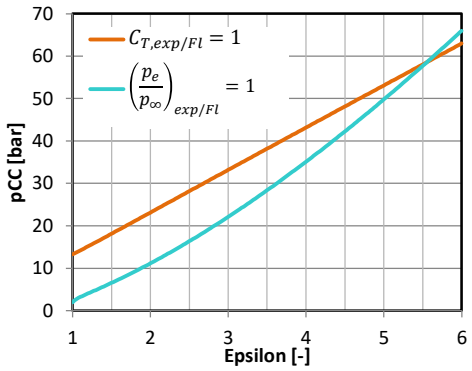

Fig. 15: Total pressure in the wind tunnel model for thrust coefficient and APR similarity as function of the model nozzle expansion area ratio for the Mach 0.4 condition

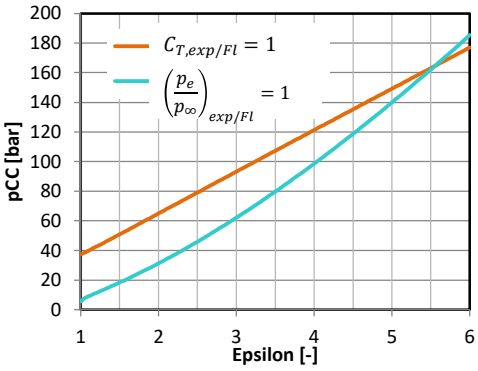

Fig. 16: Total pressure in the wind tunnel model for thrust coefficient and APR similarity as function of the model nozzle expansion area ratio for the Mach 0.8 condition

Mach	$p_{e,Fl}$ [bar]	$p_{\infty,Fl}$ [bar]	$p_{\infty,exp}$ [bar]
0.4	0.874	0.847	1.013
0.8	0.874	0.301	1.013

Tab. 1: Flight (Fl) and experimental (exp) conditions for the design of the wind tunnel model nozzles

The nozzle contour was designed for the cold gas and the hot gas experiments. It was computed with the commercially available program RPA (Rocket Propulsion Analysis), in a way that the same nozzle exit angle as in the reference engine was achieved. An ideal contour was approximated with a parabola. The ideal nozzle contour strongly depends on the heat capacity ratio, which in turn depends on the gas or combustion products used in the experiments. In RPA a shifting chemical equilibrium model is used to compute the gas composition and properties along the nozzle [14].
Due to reactions and temperature changes in the flow, the heat capacity ratio varies along the nozzle. For the hot gas experiments the OFR is the decisive factor for the heat capacity ratio. Therefore, the ideal nozzle contour was computed for air and for various OFRs of oxygen and hydrogen. They are shown in Fig. 17. Differences between the nozzle contours are observable, however, they can be considered to be small. The absolute and percentage difference in the contours compared to the contour for air is depicted in Fig. 18.
Especially for an OFR of 2.0 the differences of the contours are negligible. For other OFR the deviation is below 0.05%. Hence, the contour for air was chosen for the experiments as the deviations in general are small and an OFR of 2.0 was considered a realistic value to be achieved in the experiments. Furthermore, this is advantageous, as the same nozzle contour can be used for the cold gas and the hot gas experiments.

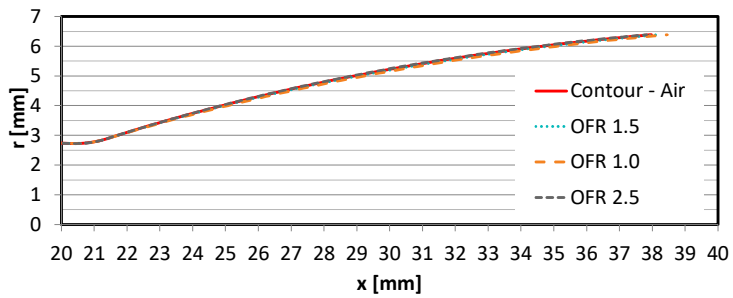

Fig. 17: Ideal nozzle contours for air and several OFRs of oxygen and hydrogen

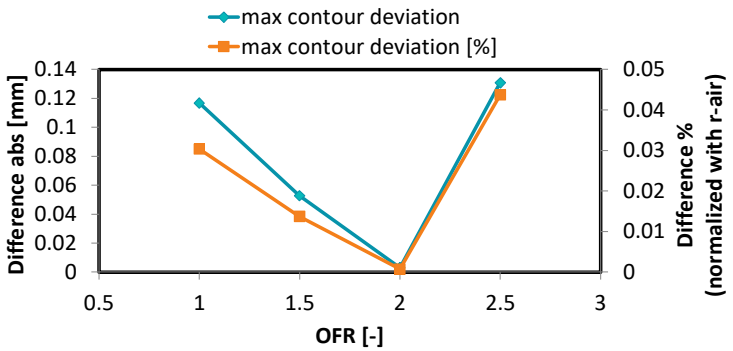

Fig. 18: Maximum deviation of nozzle contours for different OFRs of oxygen and hydrogen from the nozzle contour for air

3.5. Test Conditions

In Fig. 19 the Mach numbers tested in the wind tunnels in the frame of RETALT were mapped on the trajectory presented in [1]. Here also the test conditions of the hypersonic re-entry burn, tested in the Hypersonic Wind Tunnel Cologne (H2K) [13, 15] and of the aerodynamic phase, tested in the Trisonic Wind Tunnel Cologne (TMK) [9, 16] are shown. One can see that the descent trajectory can be represented well in the wind tunnel facilities. The detailed test conditions for the hot combustion tests are summarized in Tab. 2.

Initially the wind tunnel tests were planned with high OFRs. In the performance map of the Hot Plume Testing Facility (HPTF) (Fig. 4b), it can be seen that the range of possible OFR is large. However, as the wind tunnel model is positioned in the free stream of the wind tunnel it was limited in size. To avoid hydrogen embrittlement, the material selection for the combustion chamber is limited. Furthermore, instrumentation needs to be placed between the combustion chamber and the outer cover. Hence, due to space limitations, the combustion chamber wall thickness is limited too. In order not to reduce the wall thickness of the combustion chamber further, no cooling ducts were implemented. As the start of the ignition and the rundown phase introduce further heat loads in the combustion chamber, the OFR was limited to keep temperatures in the combustion chamber acceptable. It shall be pointed out, that in future iterations of the wind tunnel model, this limitation will be addressed and cooling shall be foreseen also for the combustion chamber. Especially for experiments with methane instead of hydrogen that are planned in upcoming experiments, the model design can be reworked, as the available materials for the combustion chamber is larger, as hydrogen embrittlement is not an issue.

Hence, an OFR of 0.7 was targeted to keep the temperatures in the combustion chamber low and an injector specifically designed for this condition was used. Furthermore, the pressure in the combustion chamber was set high enough to avoid flow separation in the engine nozzle. To estimate the critical exit pressure at which flow separation occurs, the correlation proposed by Stark and Wagner [17] was used:

$$\frac{p_{sep}}{p_a} = \frac{1}{M_{sep}} \qquad (7)$$

where p_{sep} is the pressure at which flow separation occurs, and M_{sep} is the corresponding nozzle exit Mach number.

The Mach number at the model's nozzle exit depends on the OFR as the heat capacity ratio changes with the composition of the hot gas in the nozzle. However, as can be seen in Tab. 2 this effect is small. The calculated exit pressure in the tests is above the pressure at which flow separation occurs for all tests. The Mach number was varied from 0.6 to 0.9. In run 99, the test duration was extended for Mach 0.8 as this test was intended for the comparison with CFD.

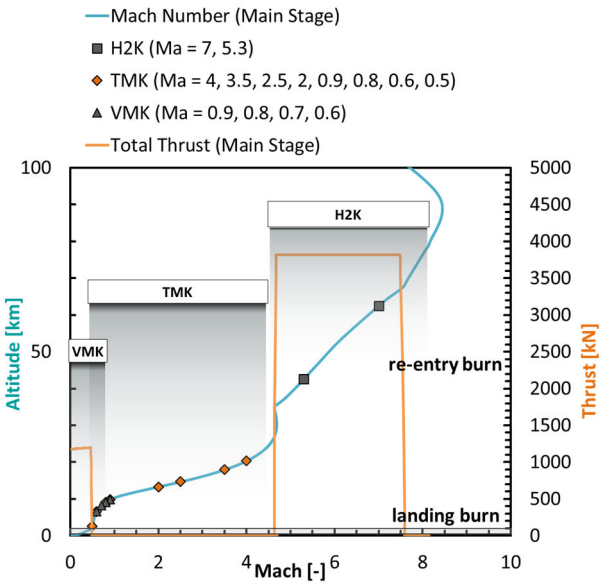

Fig. 19 Mapping of Mach numbers tested in the wind tunnel facilities at DLR in Cologne over the reference trajectory [6]

Run	Mach [-]	p_∞ [bar]	Test duration [s]	p_{CC} [bar]	$\dot{m}_{O2}$ [g/s]	$\dot{m}_{H2}$ [g/s]	OFR [-]	M_e [-]	p_e [bar]	p_{sep} [bar]	theoretical combustion temperature [K]	theoretical temperature at nozzle exit [K]	thermo-element with tcc max	tcc max [K]
90	0.6	1.020	3	20.60	19.25	29.69	0.648	3.242	0.38	0.31	880	289	tcc4	584
98	0.7	1.020	3	20.94	20.04	29.71	0.675	3.240	0.39	0.31	913	301	tcc4	700
95	0.8	1.024	3	20.45	19.06	30.6	0.623	3.243	0.38	0.31	871	286	tcc4	544
96	0.9	1.024	3	20.20	19.24	28.9	0.666	3.240	0.37	0.31	904	298	tcc4	536
99	0.8	1.021	5	21.42	19.87	29.77	0.667	3.241	0.40	0.31	905	298	tcc4	745

Tab. 2: Test conditions of performed tests

4. Results

4.1. Analysis of the flow field

The flow field was visualized with conventional cameras, an infrared camera and by high speed schlieren imaging with a frame rate of 25 kHz and an exposure time of 1.429 μs (using a continuous light source). Fig. 20 shows snapshots of the video recordings for the different test runs. It can be seen that the video recordings of all test cases are very similar to each other. In the plume a clean oxygen/hydrogen combustion is taking place, which is why the flame is bluish and barely visible [18]. Downstream of the model an orange flame is visible, which presumably comes from the mixing of the plume with the surrounding free stream air, which leads to an orange flame due to the introduction of nitrogen in the post combustion.

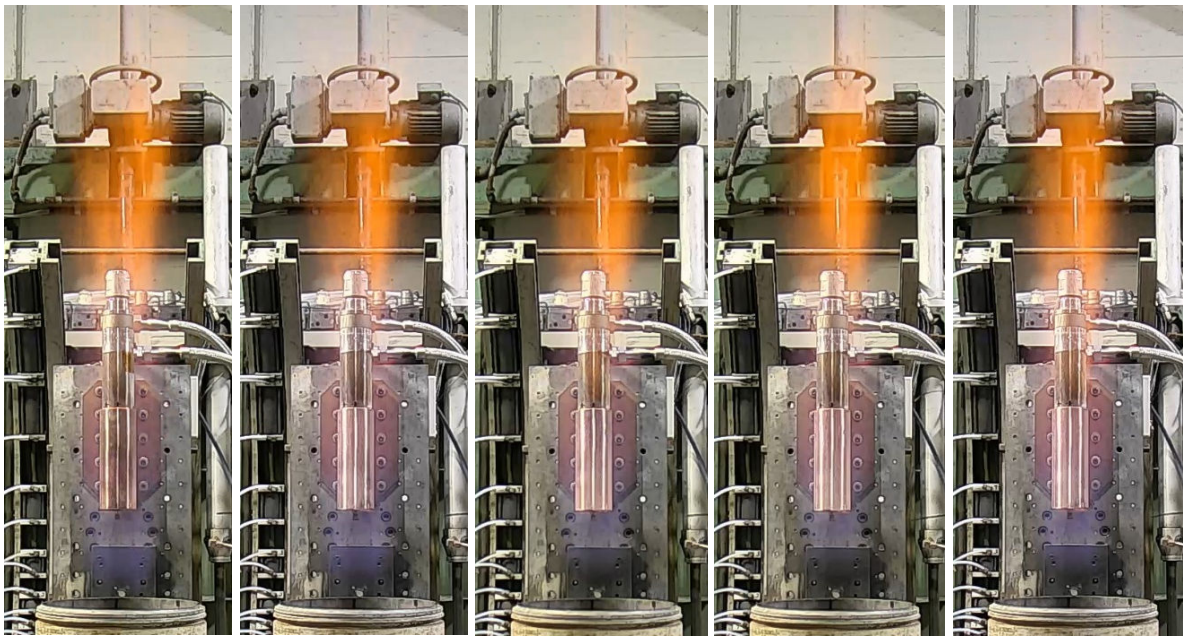

a) Mach 0.6 (run 90) b) Mach 0.7 (run 98) c) Mach 0.8 (run 95) d) Mach 0.9 (run 96) e) Mach 0.8 (run 99)

Fig. 20: Snapshots of the video recordings at the nominal condition

Fig. 21 shows the snapshots of the schlieren images and mean and variance of the schlieren videos over 2000 images with increasing Mach number. As can be seen in the snapshots, the plume shows highly turbulent structures and is very unstable.
The plume is slightly reaching into the wind tunnel nozzle in all cases. However, it can be seen that, as expected, the plume gets slimmer with increasing Mach number which indicates that the plume length decreases. This can also be seen for Mach 0.9 where the plume length coincides with the wind tunnel nozzle exit. In the mean and the variance images the structure of the overexpanded jet is clearly visible.

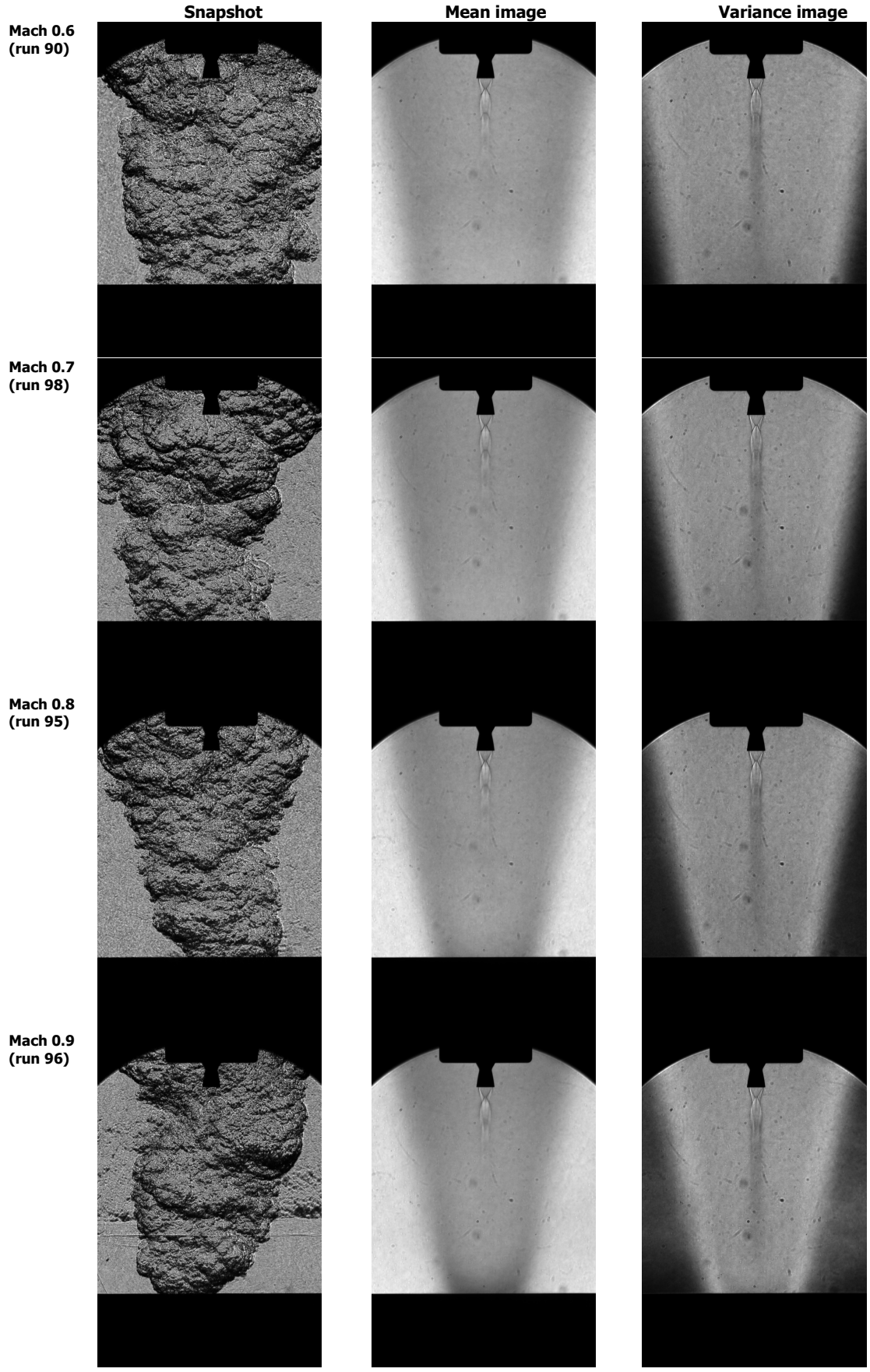

Fig. 21: Snapshots, mean image and variance over 2000 images for runs 90, 98, 95 and 96, for increasing Mach numbers of 0.6, 0.7, 0.8 and 0.9

To compare the flow topology of the hot and cold gas tests in detail, run 99 with a combustion chamber pressure of 21.4 bar at a Mach number of 0.8 was compared to the cold gas test at 22 bar at the same Mach number which was presented in [6]. Fig. 22 shows the comparison of snapshots of the Schlieren videos of the hot and the cold gas test. Due to the high density gradients of the plume with the surrounding free stream in the hot gas test due to high temperatures in the jet, the complex structures in the plume are more visible. Furthermore, the cold gas plume is shorter even though the pressure in the combustion chamber is slightly higher. The reason for this could partly be due to post combustion in the plume in the hot case which could lead to an increased extension of the plume. In general, the flow topology is quite different. The pressure waves radiating from the contact surface in the cold gas case are not visible in the hot gas case. Also, the plume in the hot gas case seems to be composed of more homogeneous turbulent structures of the same size. In the cold gas case, the flow filed is composed of the strongly unsteady jet, weaker pressure waves radiating upstream of the contact surface and larger pressure fluctuations in the wake of the jet which move in a coherent manner. In the hot gas experiments, it was furthermore observed that the plume length is relatively stable where it varies strongly in the cold gas case.

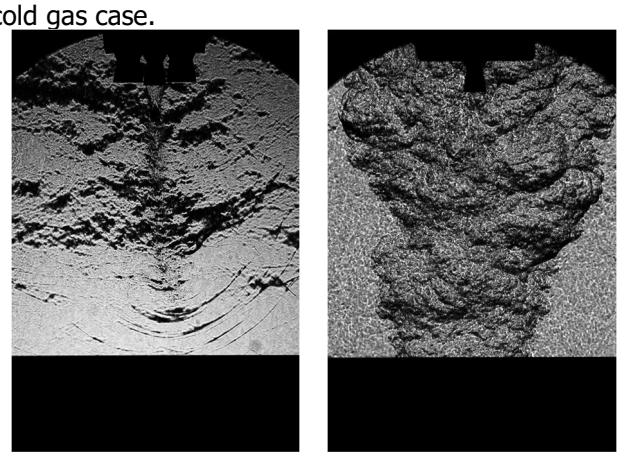

Fig. 22: Comparison of snapshots of the cold gas tests (left) at $p_{CC} = 22bar$ with run 99 of the hot gas tests with $p_{CC} = 21.4\ bar$ at OFR 0.667 (right)

A comparison of the mean flow and the variance of the Schlieren videos over 2000 images is shown in Fig. 23 and Fig. 24. In the case of the cold gas plume the highest variances can be seen in the stagnation region where the jet plume meets the free stream. In the case of the hot tests, the plume reaches slightly into the wind tunnel nozzle. The variance seems to be equally distributed in the plume region. The mean and the variance of the videos nicely reveal the shock structures emerging from the model's nozzle exit. Due to the lower exit pressure in the hot case, the plume is more overexpanded in this case.

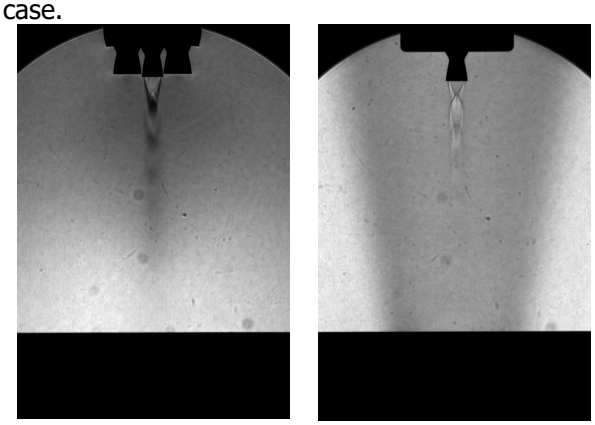

a) $p_{CC} = 22\ bar$ (cold) b) $p_{CC} = 21.4\ bar$ (hot)

Fig. 23: Comparison of mean flow of the cold gas tests (a) at $p_{CC} = 22bar$ with run 99 of the hot gas tests with $p_{CC} = 21.4\ bar$ at OFR 0.667 (b)

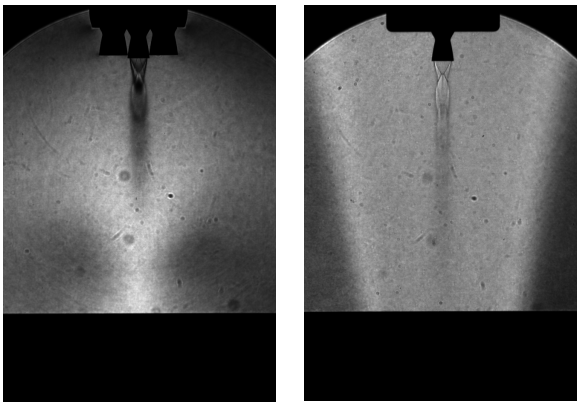

a) $p_{CC} = 22\ bar$ (cold) b) $p_{CC} = 21.4\ bar$ (hot)

Fig. 24: Comparison of the variance of the cold gas tests (a) at $p_{CC} = 22bar$ with run 99 of the hot gas tests with $p_{CC} = 21.4\ bar$ at OFR 0.667 (b)

For the recording of the infrared camera three integration times were used. The resulting images of the three integration times are depicted for run 99 in Fig. 25. The integration time in infrared imaging acts like the exposure time in photo or videography. Therefore, the clearest representation of the instantaneous flow field is seen for the shortest integration time of 0.025 ms (equivalent to an exposure time of 1/40 000).

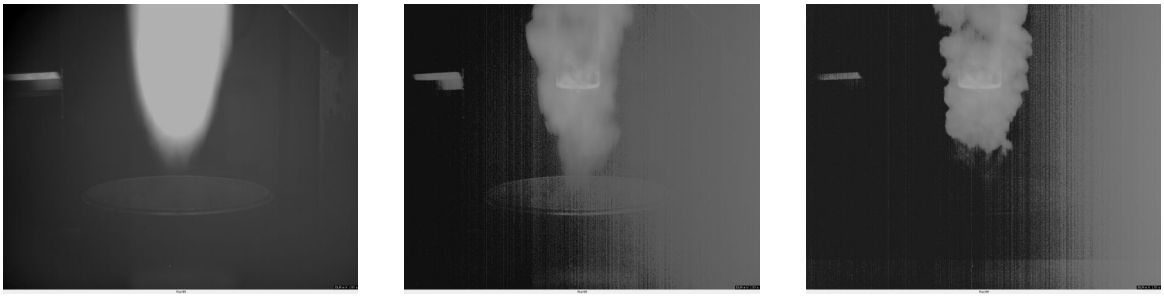

1 ms 0.1 ms 0.025 ms

Fig. 25: Infrared images of plume structure in run 99 for different integration times

To enhance the understanding of the flow field, three types of images are compared. The snapshot of the infrared video recording gives a good impression of the instantaneous flow field. However, the extend of the plume can be better assessed if the maximum image is generated. Here for every pixel the maximum value is taken over the full analyzed time window which was the time of the nominal test. The maximum image is shown in Fig. 26a. The variance over the test duration shows the fluctuation of the plume, which is shown in Fig. 26b. Fig. 27 shows the snapshot, the maximum image and the variance of the flow field for the same test condition with increasing Mach number. It can be seen that the plume, visualized like that, decreases in size with increasing Mach number. Here also the trend can be seen that the plume length decreases with increasing Mach number, which is expectable due to the dependency of the plume length on the MFR. The boundary of the jet (the fluctuating region where the variance is high) seems to have a similar extend independently of the Mach number. The plume visualized with the infrared camera is smaller than the one seen in the Schlieren images, as the outer part of the plume is colder which is why it cannot be detected. Hence, only the inner part of the plume at the contact surface of the plume with the free stream is visible. In the infrared snapshots and in the maximum images it can also be seen that the model sees the highest temperatures at the shoulder of the base, which is why the use of the redesigned cover was necessary for these tests.

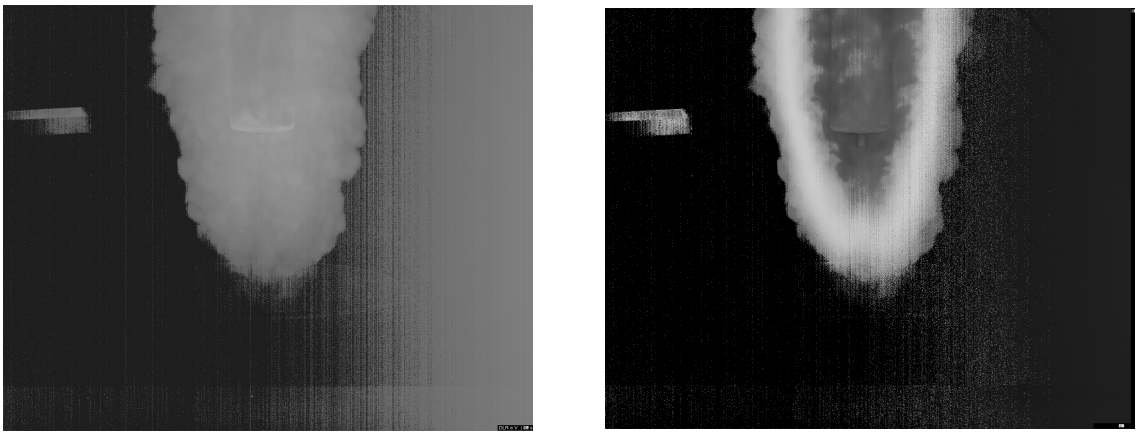

a) Maximum image b) variance

Fig. 26: Maximum image and variance of infrared recordings for run 99 (120 images)

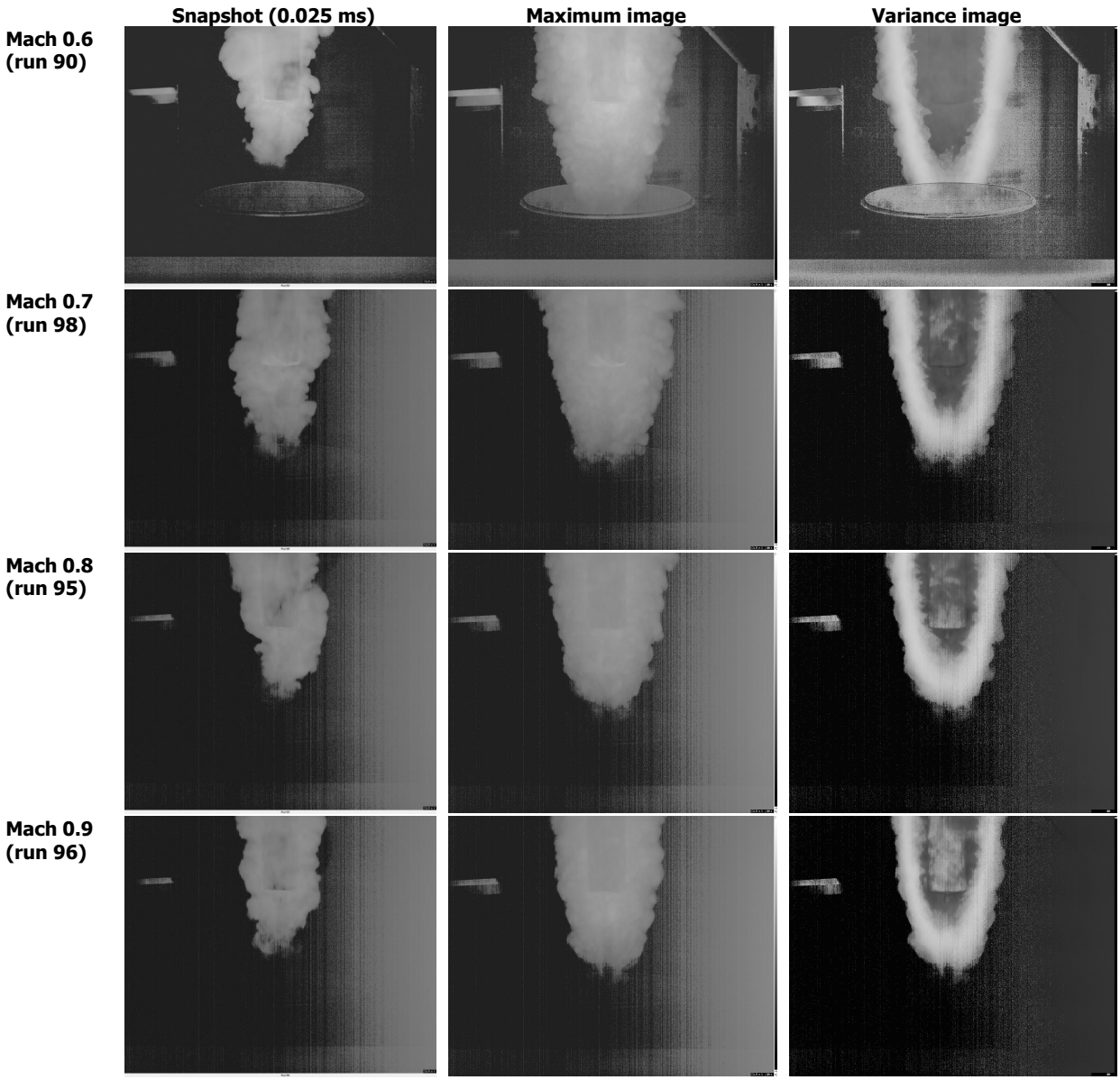

Fig. 27: Snapshots, maximum image and variance of infrared recordings for several runs with increase Mach number

As the flow field for the retro jet is highly unstable a Proper Orthogonal Decomposition (POD) was performed over 5000 images. The POD modes are shown in Fig. 28. Here the first modes mainly rebuild the outer boundary of the plume and its sideways fluctuation (mode 1 and 2). Starting from mode 6 the translational structures are covered. As for the cold case, the higher modes rebuild smaller structures (see [6] for the cold gas tests). The singular values are shown in Fig. 29. For the first modes they can be grouped into pairs of interacting modes with the same magnitude of the singular values. This is reasonable as e.g. the sideways fluctuations need several modes to be represented. However, this effect is not as pronounced as for the cold gas case (see [6]). As for the cold gas case as large number of modes is needed to recover the flow field as can be seen in the cumulative energy in Fig. 30. However, also for the hot gas case, the dominating flow features are contained in the lower modes. For example, mode 1000 does not show strongly dominating flow features anymore (see Fig. 28).

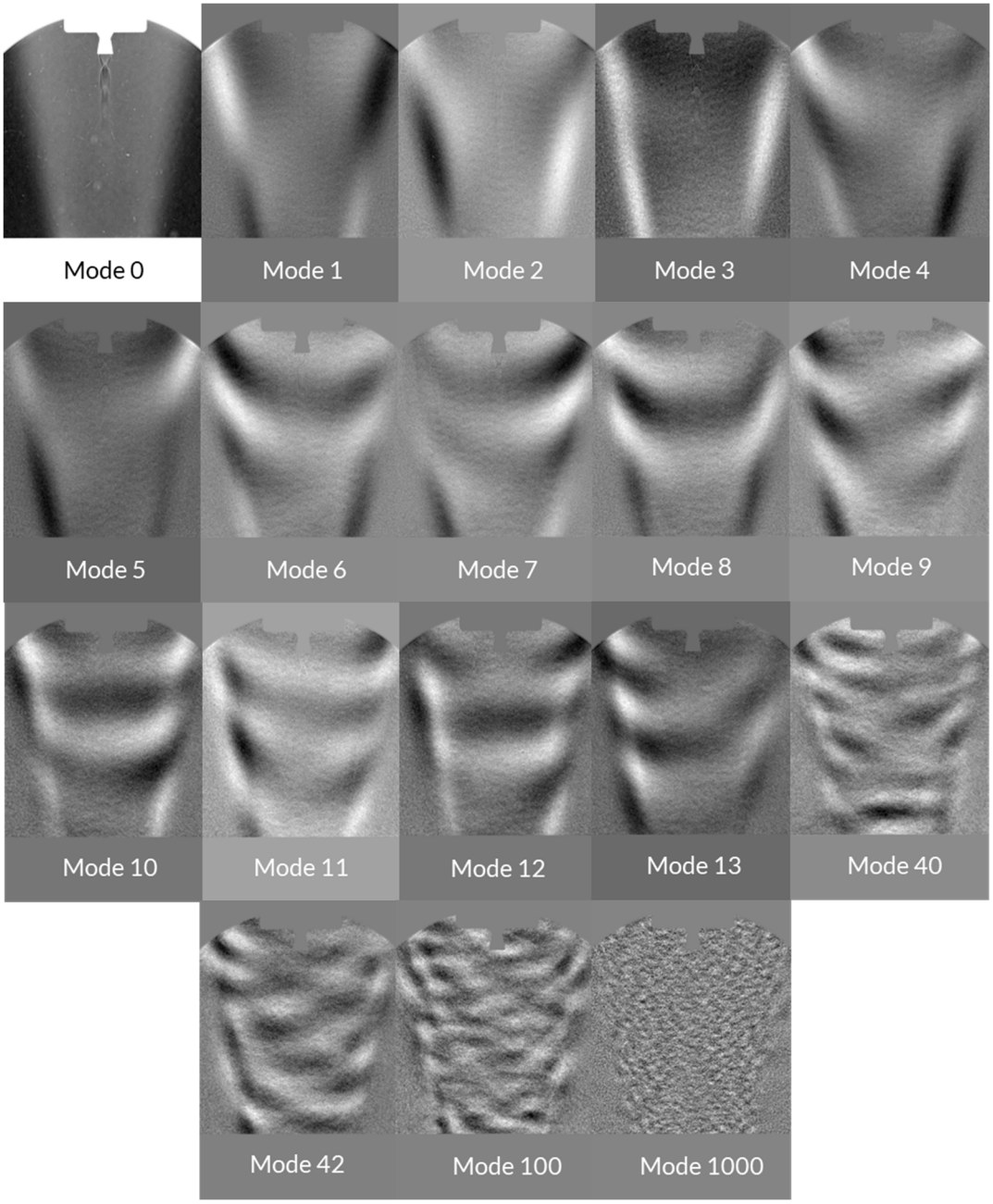

Fig. 28: Selected modes of POD of hot gas test for Mach 0.8, $p_{CC} = 21.4\ bar$ and OFR=0.667 (run99)

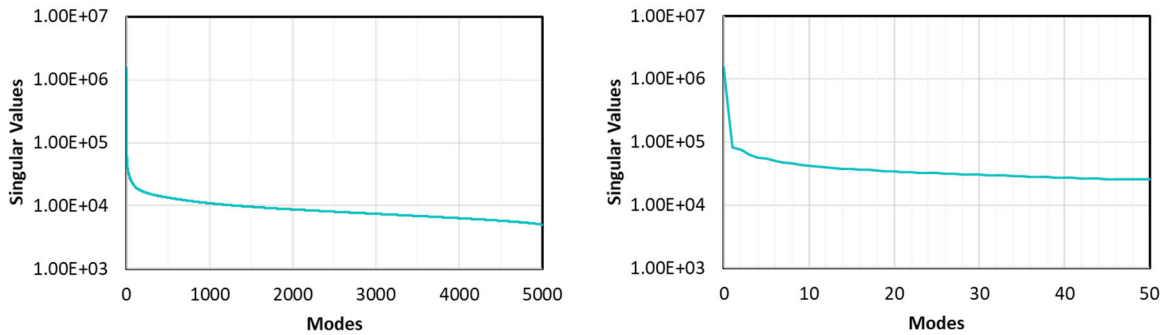

Fig. 29: Singular values versus the modes of the POD of the Schlieren images of the hot gas case (run99)

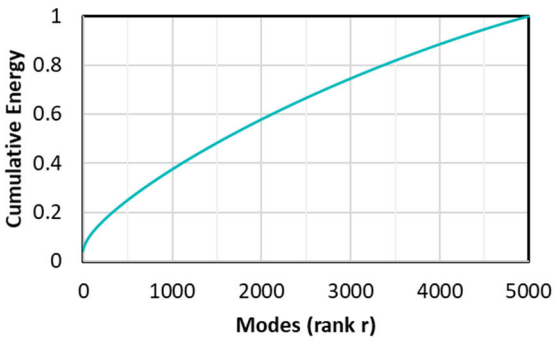

Fig. 30: Cumulative Energy versus the modes of the POD of the Schlieren images of the hot gas case (run99)

Furthermore, the Power Spectral Density of the time series of the POD modes (which are the columns of the right singular vectors of the POD) was performed and compared to the cold gas test case in Fig. 31. It shows that the tendency is in principal the same, that in both cases the lower modes are occurring at lower frequencies while higher modes occur at higher frequencies. However, the frequencies do not strictly rise with the number of the modes. Low frequencies below 3 kHz dominate the flow field of the hot case, while the cold case is dominated by frequencies lower than 4 kHz. In the hot case two prominent frequency peaks are visible at frequencies of 490 Hz and 700 Hz. The Strouhal numbers,

$$Sr_D = \frac{f D_{ref}}{u_\infty} \qquad (8)$$

corresponding to these frequencies are 0.132 and 0.188, respectively. With the frequency f the reference length D_{ref} and the free stream velocity u_∞. As for the cold gas tests in [6], the diameter of the base of 70 mm was chosen as reference length, as this makes the Strouhal numbers comparable to studies on near-wake flows of (ascending) space transportation systems where this definition was used, as e.g. in [19]. The Strouhal numbers 0.132 and 0.188 are comparable to the ones found to be dominant in the cold gas test cases of subsonic retro propulsion flow fields in general which are mostly around 0.2 [6]. However, as shown in Fig. 31 the frequencies are slightly lower and the two dominant peaks are more pronounced in the hot case.

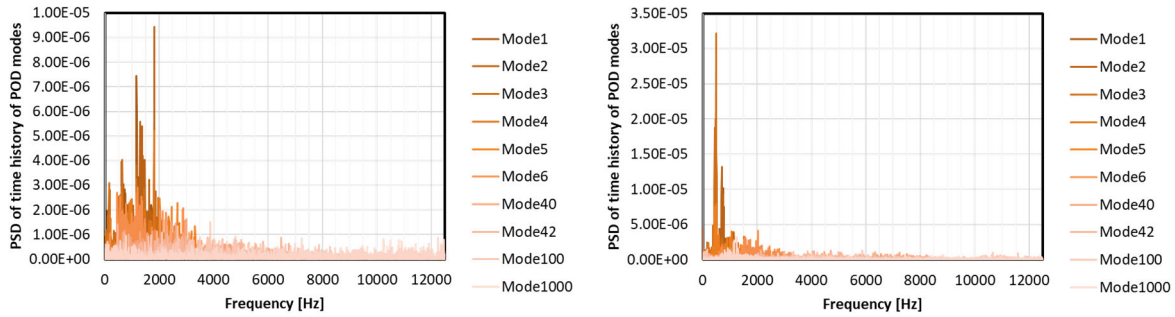

Fig. 31: Power Spectral Density of time history of the POD modes (right singular vectors) of the cold gas case (left) and the hot gas case (right)

4.2. Pressure Coefficients and temperatures for hot and cold tests

Fig. 32 shows the pressure coefficients ($C_p = (p - p_\infty)/q_\infty$) for the cold gas test with and without dummy nozzles installed. It can be observed that the pressure coefficients are nearly independent of the Mach number. The pressures in the most inner circle (02, 04, -04, 06, -06) show the highest values as they are the closest to the stagnation point. They decrease with increasing Mach number, indicating that the effect of the plume shielding the base area increases with increasing Mach number. The pressures in ring 1 are very close to the ones in ring 0 for the case without dummy nozzles installed, but smaller in the case of installed dummy nozzles as they are shielding the base area. The pressures in ring 2 (22, 24, 26, 28) which are close to the shoulder of the base area are the most independent of

the free stream Mach number if the dummy nozzles are installed. The sensors which are situated around the shoulder in the expansion of the free stream in circle 3 (30, 32, 34, 36, 38) show negative pressure coefficients due to the pressure decrease in this area. The pressure coefficients slightly decrease with the Mach number. The pressure coefficient in the sensor on the cylindrical body (L6) is positive and constant with the Mach number.
For the cases with and without installed dummy nozzles the same tendencies can be observed for the pressures in the base. However, one can observe that the magnitude of the pressure coefficients on the base area is generally slightly higher for the case without dummy nozzles due to the shielding effect of the dummy nozzles. On the other hand, the Mach number dependence is slightly higher for the case with dummy nozzles.

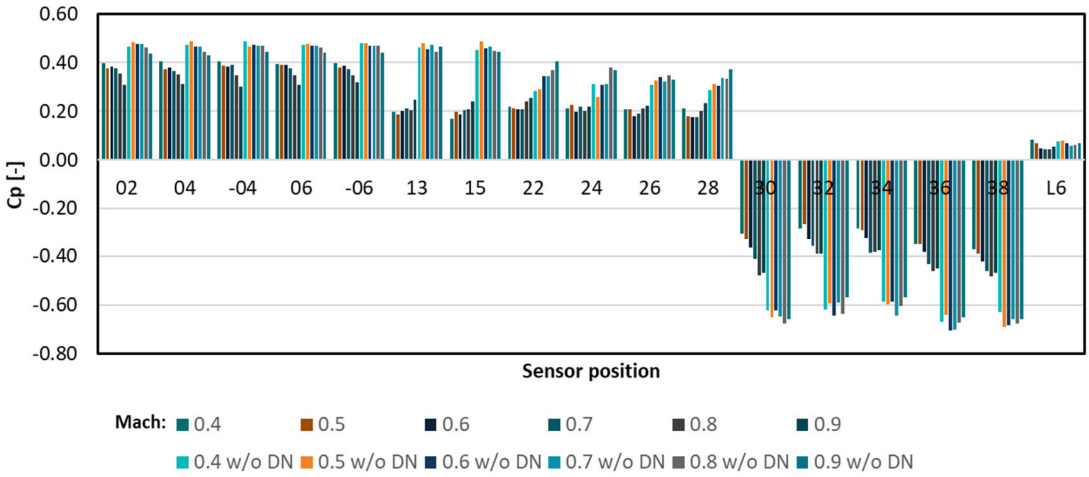

Fig. 32: Comparison of pressure coefficients for discrete Mach numbers, with and without outer nozzles (DN – Dummy Nozzles)

Fig. 33 shows the pressure coefficients at selected locations for the hot combustion tests. As for the cold gas tests the pressure coefficients on the base area are small but positive. For the first four test conditions it is observable that the pressure coefficients decrease with increasing Mach numbers. The fifth test condition with a higher pressure in the combustion chamber than the third condition at the same Mach number leads to slightly higher pressure coefficients. The pressure at 02 shows lower values for all conditions which is likely due to a slight blockage of the sensor. The pressure coefficients in the hot case are in general higher than in the cold case.

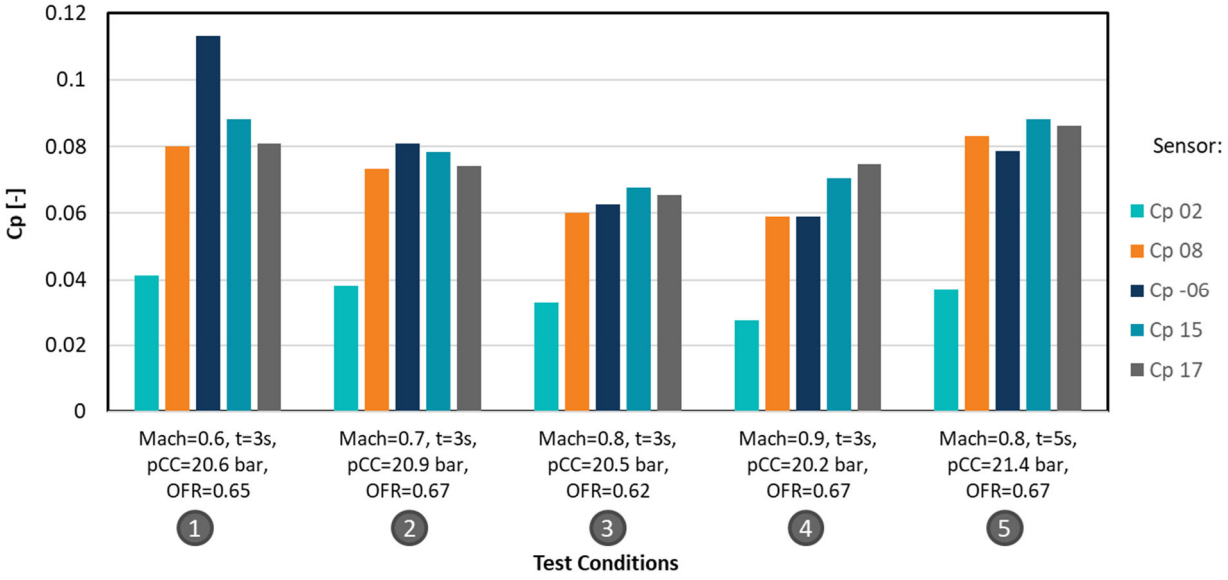

Fig. 33: Pressure coefficients for the hot combustion tests

The temperatures reached in the base during the longest run (99) are shown in Fig. 34. As the water cooling for the nozzle is also running though the base, the temperatures keep relatively low at around 400 K with a maximum of 481.5 K in sensor -25.

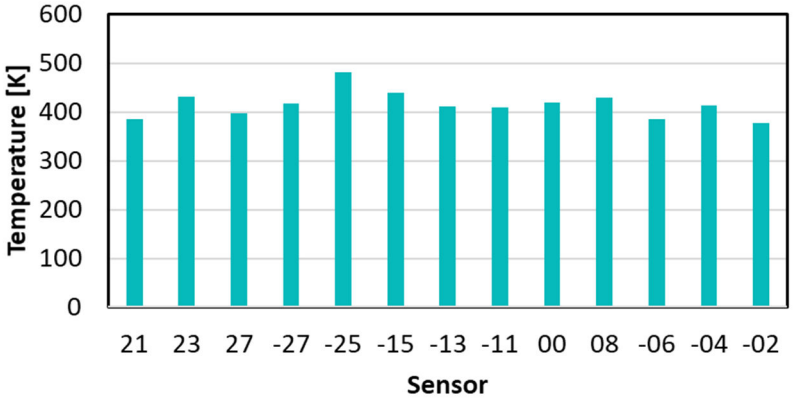

Fig. 34: Temperatures in the base area after run 99

5. Conclusions and Outlook

In this paper, first retro propulsions experiments with a wind tunnel model with oxygen/hydrogen combustion inside a model-integrated combustion chamber were presented which were performed in the Hot Plume Testing Facility (HPTF) at DLR in Cologne. The general trends known from cold gas experiments can also be found for hot gas experiments. The plume length is dependent on the momentum flux ratio and decreases with higher free stream Mach numbers if the combustion chamber pressure is kept constant. Probably also due to post combustion in the plume, the plume length is larger in the hot experiments than in the cold experiments. The plume is turbulent and shows a strongly unsteady behavior. The frequencies of the POD modes of the hot gas schlieren images are smaller than for the cold gas experiments but in the same order of magnitude. High heat loads can be observed on the outer surface of the model due to post combustion in the retro propulsion plume in which the wind tunnel model is immersed.
The design of the wind tunnel model proved to be challenging due to high heat loads on the outer cover and in the combustion chamber. To reduce heat loads in the combustion chamber the oxidizer fuel ratio was reduced to 0.7. To cope with the external heat loads a cover with a large wall thickness was designed. Due to the trends in European launcher designs towards the use of oxygen/methane engines, in future tests it is planned to perform retro propulsion tests also with oxygen/methane combustion. This change will also allow for more flexibility in the wind tunnel model design. It is expected that a combustion chamber design with 3D-printend parts made of Inconel, including cooling ducts, could lead to higher feasible OFRs and, hence, a better reproducibility of the flight conditions in the tests. Also the outer cover of the model needs to be water cooled or designed with enough heat capacity to cope with the high heat loads.

Acknowledgements

The RETALT project has received funding from the European Union's Horizon 2020 research and innovation framework program under grant agreement No 821890.

The authors would like to thank the technical staff of the VMK facility, Christian Szepanski, Viktor Hoffmann and Eddy Habegger, for their support. Furthermore, we acknowledge the effort of Markus Miketta for the wind tunnel model design.

References

[1] Marwege, A., Gülhan, A., Klevanski, J., Riehmer, J., Karl, S., Kirchheck, D., Bonetti, D., Vos, J., Jevons, M., Krammer, A., and Carvalho, J., "Retro Propulsion Assisted Landing Technologies (RETALT): Current Status and Outlook of the EU funded project on Reusable Launch Vehicles," Washington D.C., USA, 2019, https://doi.org/10.5281/zenodo.5770046.

[2] De Zaiacomo, G., Blanco Arnao, G., Bunt, R., and Bonetti, D., "Mission engineering for the RETALT VTVL launcher," *CEAS Space Journal,* Vol. 14, No. 3, 2022, pp. 533-549, https://doi.org/10.1007/s12567-021-00415-y.

[3] Botelho, A., Martinez, M., Recupero, C., Fabrizi, A., and De Zaiacomo, G., "Design of the landing guidance for the retro-propulsive vertical landing of a reusable rocket stage," *CEAS Space Journal,* Vol. 14, No. 3, 2022, pp. 551-564, https://doi.org/10.1007/s12567-022-00423-6.

[4] Ecker, T., Ertl, M., Klevanski, J., Krummen, S., and Dumont, E., "Aerothermal characterization of the CALLISTO vehicle during descent," *9 th European Conference for Aeronautics and Aerospace Sciences (EUCASS)*, Lille, Frankreich, 2022, https://elib.dlr.de/187034/.

[5] Ertl, M., Ecker, T., Klevanski, J., Dumont, E., and Krummen, S., "Aerothermal analysis of plume interaction with deployed landing legs of the CALLISTO vehicle," *9th European Conference for Aeronautics and Aerospace Sciences (EUCASS)*, Lille, France, 2022, https://elib.dlr.de/187068/.

[6] Marwege, A. and Gülhan, A., "Aerodynamic Characteristics of the Retro Propulsion Landing Burn of Vertically Landing Launchers," *Journal of Experiments in Fluids,* (accepted), https://doi.org/10.21203/rs.3.rs-3415270/v1.

[7] Korzun, A. M., Nielsen, E., Walden, A., Jones, W., Carlson, J.-R., Moran, P., Henze, C., and Sandstrom, T., "Computational Investigation of Retropropulsion Operating Environments with a Massively Parallel Detached Eddy Simulation Approach," *ASCEND 2020*, 2020, https://doi.org/10.2514/6.2020-4228.

[8] Jarvinen, P. O. and Hill, J. A. F., "Penetration of retrorocket exhausts into subsonic counterflows," *Journal of Spacecraft and Rockets,* Vol. 10, No. 1, 1973, pp. 85-86, https://doi.org/10.2514/3.27737.

[9] Marwege, A., Hantz, C., Kirchheck, D., Klevanski, J., Vos, J., Laureti, M., Karl, S., and Gülhan, A., "Aerodynamic Phenomena of Retro Propulsion Descent and Landing Configurations," *2nd International Conference on Flight Vehicles, Aerothermodynamics and Re-entry Missions and Engineering*, Heibronn, Germany, 2022, https://doi.org/10.5281/zenodo.6783922.

[10] Kirchheck, D., Saile, D., and Gülhan, A., "Rocket Wake Flow Interaction Testing in the Hot Plume Testing Facility (HPTF) Cologne," *Future Space-Transport-System Components under High Thermal and Mechanical Loads: Results from the DFG Collaborative Research Center TRR40*. Springer International Publishing, Cham, 2021, pp. 145-162, https://doi.org/10.1007/978-3-030-53847-7_9.

[11] Mejia, N. A. and Schmidt, B. E., "Experimental Investigation of Flow Interaction Dynamics in Supersonic Retropropulsion," *Journal of Spacecraft and Rockets,* Vol. 59, No. 5, 2022, pp. 1753-1762, https://doi.org/10.2514/1.A35228.

[12] Jarvinen, P. O. and Adams, R. H., "The aerodynamic characteristics of large angled cones with retrorockets," CR-124720, NASA, 1970, https://ntrs.nasa.gov/citations/19720005324.

[13] Marwege, A., Kirchheck, D., Klevanski, J., and Gülhan, A., "Hypersonic retro propulsion for reusable launch vehicles tested in the H2K wind tunnel," *CEAS Space Journal,* Vol. 14, No. 3, 2022, pp. 473-499, https://doi.org/10.1007/s12567-022-00457-w.

[14] Ponomarenko, A., *Rocket Propolsion Analysis*, User Manual, Version 2.2, 2015, http://w.lpre.de/manual/index.htm.

[15] Marwege, A. and Gülhan, A., "Unsteady Aerodynamics of the Retropropulsion Reentry Burn of Vertically Landing Launchers," *Journal of Spacecraft and Rockets,* Vol. 0, No. 0, 2023, pp. 1-15, https://doi.org/10.2514/1.A35647.

[16] Marwege, A., Hantz, C., Kirchheck, D., Klevanski, J., Gülhan, A., Charbonnier, D., and Vos, J., "Wind tunnel experiments of interstage segments used for aerodynamic control of retro-propulsion assisted landing vehicles," *CEAS Space Journal,* Vol. 14, No. 3, 2022, pp. 447-471, https://doi.org/10.1007/s12567-022-00425-4.

[17] Stark, R. and Wagner, B., "Experimental study of boundary layer separation in truncated ideal contour nozzles," *Shock Waves,* Vol. 19, No. 3, 2009, pp. 185-191, https://doi.org/10.1007/s00193-008-0174-6.

[18] Moskalenko, N. I., Zaripov, A. V., Loktev, N. F., and Ilyin, Y. A., "Emission characteristics of hydrogen-oxygen flames," *Journal of Applied Spectroscopy,* Vol. 77, No. 3, 2010, pp. 378-385, https://doi.org/10.1007/s10812-010-9342-4.

[19] Saile, D., *Experimental Analysis on Near-Wake Flows of Space Transportation Systems*, Forschungsbericht, Vol. 04, Rheinisch-Westfälische Technische Hochschule Aachen (RWTH), Aachen, 2019, https://elib.dlr.de/130993/.